Acta Materialia 199 (2020) 19–33

Contents lists available at ScienceDirect

Acta Materialia

journal homepage: www.elsevier.com/locate/actamat

Full length article

Origin of dislocation structures in an additively manufactured austenitic stainless steel 316L

K.M. Bertsch[a,b,c,*], G. Meric de Bellefon[a,b], B. Kuehl[a,b], D.J. Thoma[a,b]

[a] Department of Materials Science and Engineering, University of Wisconsin-Madison, 1550 Engineering Dr., WI 53706, USA
[b] Grainger Institute for Engineering, University of Wisconsin-Madison, Madison, WI 53706, USA
[c] Lawrence Livermore National Laboratory, Livermore, CA 94550, USA

ARTICLE INFO

Article history:
Received 24 May 2020
Revised 27 July 2020
Accepted 28 July 2020
Available online 14 August 2020

Keywords:
Additive manufacturing
Dislocations
Dendrites
Transmission electron microscopy
Orientation mapping

ABSTRACT

In this experiment, the origin of dislocation structures in AM stainless steels was systematically investigated by controlling the effect of thermal stress through geometric constraints for the first time. Stainless steel 316L parts were produced in the form of "1D" rods, "2D" walls, and "3D" rectangular prisms to evaluate the effect of constraints to thermal expansion/shrinkage on the development of defect microstructures and to elucidate the origin of additively manufactured (AM) dislocation microstructures. Dislocation density, organization, chemical micro-segregation, precipitate structures, and misorientations were analyzed as a function of increasing constraints around solidifying material in 1D, 2D, and 3D components built using both directed energy deposition (DED) and powder-bed selective laser melting (SLM). In DED parts, the dislocation density was not dependent on local misorientations or micro-segregation patterns, but evolved from approximately $\rho_{\perp} = 10^{12} m^{-2}$ in 1D parts to $\rho_{\perp} = 10^{14} m^{-2}$ in 3D parts, indicating that it is primarily thermal distortions that produce AM dislocation structures. In DED 3D parts and SLM parts, dislocation densities were highest ($\rho_{\perp} \approx 10^{14}$ m^{-2}) and corresponded to the formation of dislocation cells approximately 300-450 nm in diameter. Dislocation cells overlapped with dendrite micro-segregation in some but not all cases. The results illustrate that dendritic micro-segregation, precipitates, or local misorientations influence how the dislocations *organize* during processing, but are not responsible for *producing* the organized cell structures. This work shows that AM dislocation structures originate due to thermal distortions during printing, which are primarily dictated by constraints surrounding the melt pool and thermal cycling.

1. Introduction

Metal additive manufacturing (AM) allows for greater design freedom than conventional fabrication methods [1–3]. In addition, AM fabrication of stainless steel (SS) 316L has been shown to produce material with a combination of both high strength and ductility that is not typically observed in conventionally-processed SS 316L [4–6]. The improved mechanical properties have been attributed to grain boundary strengthening [7] or, more frequently, to dislocation cell structures with solute micro-segregation that develop in AM metals [6,8]. Elucidating the mechanism of formation of these dislocation structures can enable better control over the microstructure of AM metals and alloys for property optimization. Several potential mechanisms for the formation of these AM dislocation structures have been proposed [4,9] and are briefly described below.

In the first proposed mechanism, constitutional stresses arising due to solute enrichment that develops in inter-dendritic regions during directional solidification induce distortions that are accommodated by dislocations [8,10]. The magnitude of the constitutional stresses is dependent on the magnitude of micro-segregation and the segregating species. Dislocation densities in AM steels have been estimated to be approximately 10^{13}–10^{14} m^{-2} [4,7,11-13]. These dislocation densities are orders of magnitude higher than the densities induced by the constitutional stresses accompanying the micro-segregation developed during directional solidification of e.g. Cu (on the order of 10^{11} m^{-2}) [11]. This suggests that the micro-segregation in AM cell walls may be insufficient to generate all of the observed dislocations.

In another proposed mechanism, the fine, distributed precipitates that are typically present along the enriched inter-dendritic regions are proposed to introduce coherency strains and misfit

* Corresponding author.
E-mail address: bertsch5@llnl.gov (K.M. Bertsch).

https://doi.org/10.1016/j.actamat.2020.07.063
1359-6454/

dislocations [14]. The formation of these dislocations has been proposed to contribute to the observed dislocation densities, and to act as a network of barriers to subsequent dislocation motion thereby dictating the overall dislocation structure.

Yet another proposed mechanism claims that misorientations between dendrites are accommodated by interfacial, “geometrically necessary” dislocations (GNDs), which lock in the dislocation structure spacing to that of the dendrites [5,15]. Boundaries made up of these GNDs, or geometrically necessary boundaries (GNBs), are detectable using orientation analysis and would be expected to act as obstacles to subsequent mobile dislocations. In this mechanism, dislocation networks are suggested to originate during solidification due to constitutional stresses, precipitate networks, or interdendritic misorientations, which sets up a framework for any dislocations formed after solidification to organize around.

In a fourth mechanism, it has been suggested that thermal expansion and contraction after solidification and during rapid, local heating and cooling cycles introduces significant plastic strain [11,16–18]. In this case, contrary to the first three mechanisms, dislocations nucleate due to thermal distortions after solidification, and subsequently interact with dendrite micro-segregation patterns, precipitate networks, or interdendritic misorientation networks. The majority of proposed mechanisms in the literature assume that some amount of the dislocation content is produced by thermal distortions, but propose different mechanics for the nucleation of the initial dislocations and for the alignment/organization of structures as they evolve.

A final proposed mechanism suggests that the dislocation cells form first due to thermal stresses, and chemical micro-segregation occurs to dislocation walls later [18]. However, this theory that segregation occurs after dislocation cell formation does not address the alignment of micro-segregation patterns with dendrites (along {001} planes in cubic materials) [19]. The dendritic nature of the cell networks suggests the chemical micro-segregation occurs during solidification instead of after.

Despite extensive observation of AM SS 316L dislocation structures in the literature, the majority of experiments are designed to evaluate the effects of these structures on material response, such that many questions remain regarding the origin of these structures. In this study, we implement a novel experimental approach to test the validity of the postulated mechanisms by separating thermal stress effects from solidification effects on dislocation structure development.

The freedom afforded by AM allows for the reduction of geometrical constraints surrounding solidifying material. Printing with directed energy deposition (DED) allowed for the creation of “1D” rods by moving the print head continuously upwards in the build direction. In these "1D" parts, the only physical constraint present to resist thermal contraction of material after solidification existed at the bottom of the rod, with the remainder of the material free to shrink upon cooling in any direction. In “2D” walls, the solidifying material was constrained by existing solid material from both the bottom of the melt pool and in the scanning direction behind the melt pool, but not in the through-thickness dimension of the wall. In "3D" parts, the solidifying material became constrained in the build direction, opposite the scanning direction, and additionally in the through-thickness direction since the melt pool penetrated previous layers and adjacent hatches.

A similar part design was adopted using powder-bed selective laser melting (SLM), where a bed of metal powder is swept over the build plate to build up each layer, to investigate the generality of results obtained for DED. In SLM, the geometric constraints could not be eliminated as completely as in DED since the process is necessarily discontinuous. However, reducing the amount of surrounding material to create quasi-1D and -2D parts allowed for analysis of the effect of increasing constraints in a qualitative manner in SLM parts for comparison to DED.

The systematic elimination of geometric constraints allowed for systematic manipulation of the thermal stresses in a new way., which was critical to definitively identify the driving force for AM dislocation structure formation.

Table 1
Chemical compositions of SLM and DED parts in wt%.

	Cr	Ni	Mn	Si	C	Cu	N	O
SLM	18.39	13.94	1.47	0.3	0.004	0.0022	0.065	0.043
DED	18.06	13.79	1.58	0.32	0.005	0.0095	0.072	0.037

2. Experimental Procedure

2.1. Printing

2.1.1. Directed energy deposition

An Optomec Laser Engineered Net Shaping (LENS) MR-7 unit was used to fabricate DED parts, with SS 316L powder (45–150 μm) supplied by Carpenter®. The scanning strategies utilized for the different geometries are shown in Fig. 1.

Laser scanning directions are indicated by arrows. Build direction is vertical.

1D rods were built by continuously moving the print head directly upwards in the build direction after turning on the laser. Material was added continuously under the 600 µm laser spot until a rod 25 mm tall was built. Parameters included a laser power 200 W and a vertical print head velocity of 1.5 mm/s.

The 2D walls were built semi-continuously such that each layer consisted of a single track with a snake scan strategy to move between layers, e.g. each new track began where the previous track ended, as shown in Fig. 1. Walls were 25 mm wide x 25 mm tall, with print parameters of laser power 400 W, laser scan speed 8.5 mm/s, and layer spacing 0.254 mm. Different laser powers and scan speeds than used for the 1D rod were necessary, since the laser power and speed that allowed for continuous building of 2D walls did not successfully create 1D rods and vice versa. 1D rods and 2D walls were printed onto standard 316L base plates.

The 3D rectangular prism geometry was 50 mm long x 10 mm wide x 3 mm tall, with a hatch spacing of 0.35 mm and a snake scan strategy between passes within the same layer, as indicated in Fig. 1. A contour deposit was made to outline each new layer, and each layer was rotated 90° relative to the previous layer scan direction. Laser power 275 W, scan speed 8.5 mm/s, and layer thickness 0.254 mm were used for 3D components. The 3D prism was printed onto a 316L base plate that had been cold-rolled to 80% thickness reduction and solution-annealed in an Ar atmosphere at 1050°C for one hour prior to deposition to remove preexisting defect structures.

Chemical analysis was used to analyze the printed material composition in the 3D parts, as shown in Table 1.

2.1.2. Selective laser melting

SLM parts were manufactured in an EOS M290 laser powder-bed fusion unit using SS 316L powder (15-45 μm) provided by EOS®. The powder-bed SLM process required SLM 1D rods to be built layer-by-layer (instead of continuously), with each layer represented by a single “point”. Since the EOS printing software slices parts into representative triangles, each “point” layer consisted of a triangle with sides 100 µm. The triangles were approximately the same size as the laser beam diameter (nominally 80 µm), such that each triangle ended up as a single point during the deposition. Thus, the print speed effectively dictated the laser dwell

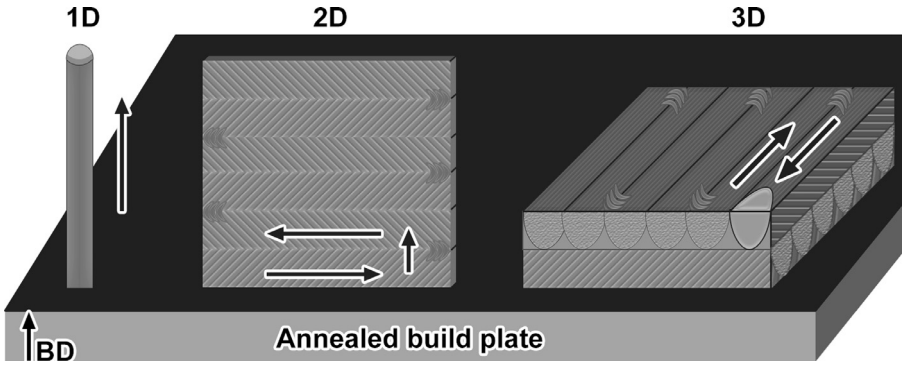

Fig. 1. Schematic illustrating laser scan strategy and geometry for DED 1D, 2D, and 3D parts. Laser scanning directions are indicated by arrows. Build direction is vertical.

time for each layer of the 1D rods. 1D rods were built 13 mm tall, with 100 W laser power, 775 mm/s scan speed, and layer thickness of 0.02 mm. Additionally, a support structure 5 mm tall was deposited between the build plate and the SLM rods (as well as other SLM parts) for easier removal.

SLM 2D walls were built with laser power 100 W, scan speed 675 mm/s, and layer thickness 0.02 mm. Walls typically exhibited large distortions due to residual stresses, particularly near the ends of the walls, and frequently did not build completely up to the desired height. The wall selected for dislocation structure analysis was built up to the desired 13 mm height. The area selected for transmission electron microscopy (TEM) foil extraction was in the middle of the wall, away from the obvious distortions.

SLM 3D prisms 3 mm tall were built using standard print parameters recommended by EOS for SS 316L, with laser power 195 W, scan speed 1083 mm/s, and layer thickness 0.02 mm. The scan strategy was the same as that used with the DED parts, but with hatch spacing of 0.09 mm and a necessarily larger number of layers to build up an equivalent amount of material.

Chemical analysis of SLM and DED 3D parts revealed similar bulk compositions across the two methods, with no compositional differences greater than 0.3 wt%, as shown in Table 1.

2.2. Preparation and microscopy

Specimens were removed from build plates using a low speed saw or manually, except for one DED 3D prism. This DED 3D prism was left on the build plate and sectioned perpendicular to the long axis for analysis of the microstructure across the base plate interface. This allowed for direct comparison of melted/resolidified regions with unmelted regions that experienced identical local thermal and strain histories in the DED 3D material. Specimens (including the sectioned base plate specimen) were mounted in epoxy and mechanically polished down to a 0.05 µm grit silica solution, then electrolytically etched with 0.05 M oxalic acid solution at approximately 6 V for 60 s each, such that any mechanical damage layer was effectively removed. Analysis of the dendrite structures revealed by etching was performed in either a Zeiss LEO 1530 Gemini field emission scanning electron microscope (SEM) operated at 5 kV or a FEI Helios G4 plasma focused ion beam (PFIB) CXe with an Elstar^{TM} SEM column operated at 5 kV.

Thin foils for transmission electron microscopy (TEM) analysis were extracted using FIB machining in the FEI Helios PFIB and a Zeiss Auriga model Ga FIB. Foils were extracted across primary dendrite arms. A protective Pt layer was applied during the FIB machining process to preserve surface topography created by etching; the Pt layer was edited out of images for clarity. Secondary dendrite arm spacing (SDAS) and cooling rates were measured near the locations selected for TEM analysis. For the DED 3D part, a specimen was extracted that extended across primary dendrite arms in the deposited AM material and across the interface with the annealed base plate. Additional TEM specimens were extracted from DED and SLM 3D parts by mechanically grinding parts into foils less than 200 µm thick, then punching out 3 mm TEM disks. Disks were polished to electron transparency using a Struers Tenupol Twin-Jet polisher with A2 solution at -20°C and 12 V for approximately 15 min.

Scanning TEM (S/TEM) analysis of the defect microstructures was performed in an FEI Tecnai TF-30 S/TEM operated at 300 kV and in an FEI Titan 80–200 aberration-corrected TEM operated at 200 kV. Bright field (BF) imaging was performed using the diffraction contrast STEM technique with a [011] zone-axis beam direction unless otherwise noted. Specimens with multiple grains were imaged with each grain at a [011] zone axis condition at different tilt angles, and montages were stitched together such that the physical appearance of the grain boundaries was maintained. Orientation mapping of the foils was performed using transmission electron backscatter diffraction (t-EBSD) in the Helios PFIB equipped with an Hikari camera, with step sizes approximately 40 nm and operating voltage 25–30 kV. Orientation analysis was performed utilizing the MTEX software package [20] and MATLAB functions.

Energy dispersive spectroscopy (EDS) analysis was performed across dislocation structures in DED specimens in the Titan S/TEM using a 128 eV-resolution detector. The purpose of EDS mapping was to confirm that interdendritic micro-segregation was present in the DED material and that the spacing of the micro-segregation observed in TEM specimen microstructures corresponded to the dendrite spacing observed on surfaces after etching. In SLM SS 316L material, micro-segregation has previously been shown to overlap with both primary dendrite arms observed on etched/polished surfaces as well as with internal dislocation cell structures [5,6,10,18]. In this study, dendrites were observed on etched surfaces with the same spacing as dislocation structures. This was considered sufficient to confirm the presence of interdendritic micro-segregation at dislocation cell walls in SLM specimens, and it was not considered necessary to perform EDS mapping for SLM materials.

3. Results

3.1. Dendrite arm spacing and cooling rates

Primary and secondary dendrite arms were observed in all specimens upon etching. The dendrite structures are shown in the SEM images of Fig. 2, with the locations from which cross-sectional TEM specimens were extracted via FIB indicated by black rectangles.

When etched, SS 316L material with interdendritic micro-segregation forms protrusions at the interdendritic regions be-

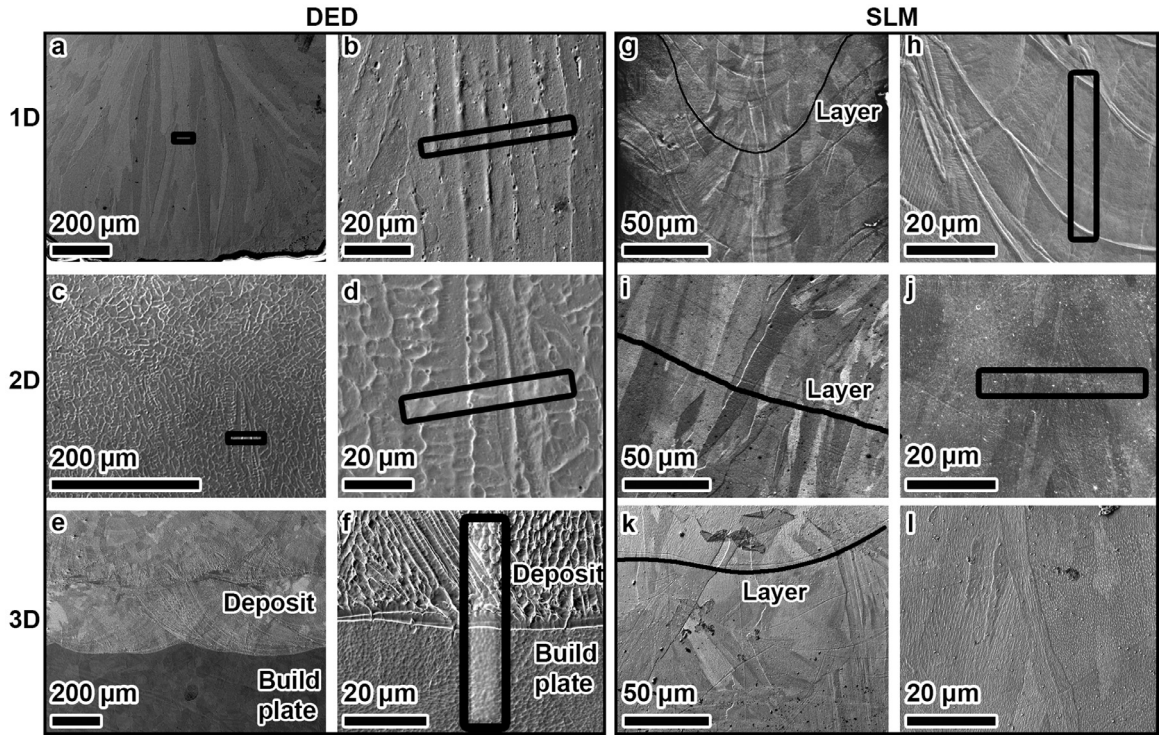

Fig. 2. SEM of microstructures for a-f, DED specimens, and g-l, SLM specimens. Boxes indicate FIB liftout locations; build direction is vertical. FIB extraction was not used to prepare TEM specimens in SLM 3D material.

Table 2
Primary dendrite arm spacing (PDAS) measured for TEM lamellae extracted via FIB machining for dislocation structure analysis.

	DED			SLM		
	1D	2D	3D	1D	2D	3D
PDAS [μm]	6.5 +/-0.1	5.8 +/-0.8	Base: 1.9 +/-0.3 Center: 2.2 +/-0.3	0.27 +/-0.04	0.39 +/-0.1	0.46 +/-0.1

tween primary dendrite arms due to the different local chemistry. In this study, dendrite arms are enriched in Cr, Mn, and Mo, and somewhat depleted in Fe, indicating enhanced resistance of the interdendritic regions to chemical etching relative to the matrix [18,21]. These interdendritic regions are typically referred to as dendrite arms, even though the primary dendrite is actually the region between these protrusions. FIB milling of etched surfaces confirmed that dendrite arms corresponded to surface protrusions in this study. Subsequently, surface protrusions observed in TEM specimens extracted via FIB are said to indicate the location of dendrite arms in the current work. The average primary dendrite arm spacing (PDAS) for each specimen geometry is shown in Table 2.

SDAS was measured from SEM images for each specimen. These measurements allowed for calculation of the cooling rate via the following relationship:

$$\lambda_2 = B\ \dot{\varepsilon}^{-n} \tag{1}$$

where λ_2 is the SDAS in µm, $\dot{\varepsilon}$ is the cooling rate in K/s, and the constants B = 25 and n = 0.28 for SS 316L [22–24]. For each specimen, measurements were taken from at least five different areas of the specimen, and each measurement consisted of an average spacing between at least seven consecutive secondary dendrite arms. Cooling rates calculated from SDAS measurements varied over several orders of magnitude across the different materials and geometries, as shown in Table 3. Note that the SDAS listed in Table 3 is different than the PDAS listed in Table 2 and illustrated in Fig. 2.

Cooling rates for DED 1D rods and 2D walls were calculated from SDAS measurements taken within 0.5–1 mm of the base plate, near the sites of extraction of TEM lamellae. These locations were selected for analysis in order to compare the microstructures that formed in regions with cooling rates that were as close as possible to those observed in the 3D DED parts. For the DED 3D parts, microstructural analysis of dislocation structures was performed both near the base plate and at the center of the part, so cooling rates for both locations are given in Table 3. In SLM parts, measurements were taken approximately 7–10 mm from the base plate (2–5 mm from the end of the support structures).

In the following, the results for each specimen are presented in order of dislocation density and structures first, followed by the correlation of dislocation structures with dendrite microsegregation profiles, precipitate structures, and lastly local misorientations.

3.2. DED microstructures

3.2.1. DED 1D

TEM specimens for DED 1D rods were extracted across primary dendrites approximately 450 µm from the bottom of the rod, as shown in Fig. 2a and b. The dislocation structure of the 1D rod material is shown in the bright-field diffraction-contrast STEM image Fig. 3a. Multiple grains were captured in the foil, as indicated

Table 3
Cooling rates [K/s] measured from SDAS for regions analyzed with TEM.

	DED			SLM		
	1D	2D	3D	1D	2D	3D
SDAS [μm]	2.9 +/-0.4	3.0 +/-0.1	Base: 1.0 +/-0.2 Center: 1.1 +/-0.1	0.24 +/-0.04	0.23 +/-0.04	0.26 +/-0.04
Cooling rate [K/s]	3 x 10^3	2 x 10^3	Base: 1 x 10^5 Center: 7 x 10^4	2 x 10^7	2 x 10^7	1 x 10^7

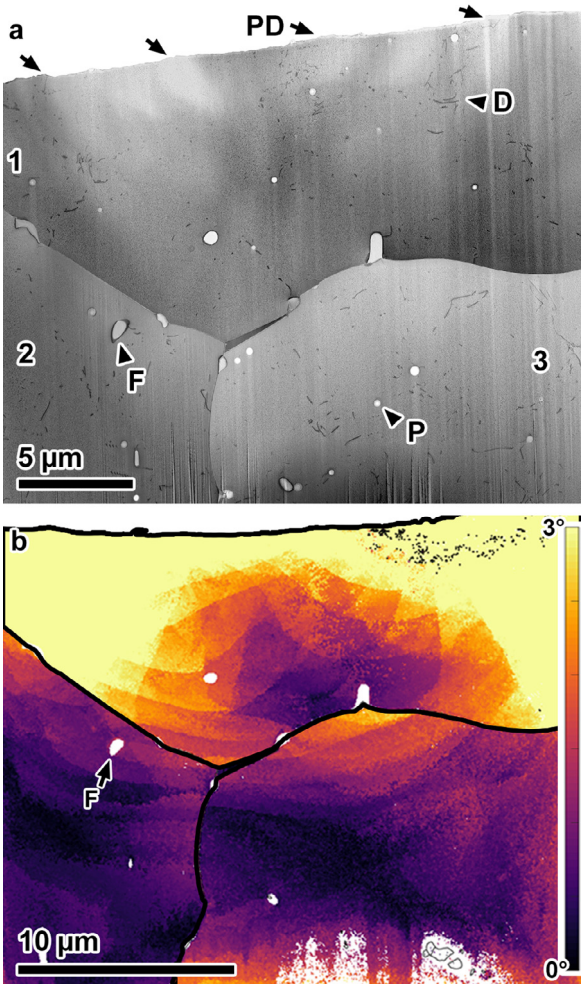

Fig. 3. a. Bright-field zone-axis STEM of defect structures in DED 1D rod. Surface protrusions due to etching of regions with interdendritic micro-segregation are labeled PD and indicated by arrows. Ferrite inclusions, oxide precipitates, and dislocations indicated by "F", "P", and "D", respectively. Different grains labeled 1, 2, and 3. b. t-EBSD misorientation map of the grains shown in a. Color online.

by the sharp background contrast changes across grain boundaries; grains are labeled 1–3 for clarity. Dislocations were sparse and typically isolated in the 1D rod structures, for example near the arrowhead labeled "D" in Fig. 3, with no organization into cell structures.

Line-intercept analysis of the dislocation density [25] suggested a density on the order of 2 x 10^{12} m^{-2} for a foil thickness of approximately 200 nm (measured via edge-on SEM imaging). This method is subject to inaccuracies due to projection effects, loss of dislocations during sample preparation, and inaccuracies in measuring foil thickness [26], such that we consider these measurements to have an error range of within an order of magnitude. Dislocation densities are tabulated in Table 4.

Surface protrusions corresponding to primary dendrite arms are labeled PD and indicated by arrows in Fig. 3a. The dendrites are seen in the SEM image of Fig. 2b. EDS analysis was performed along a line perpendicular to the primary dendrite arms direction to define the interdendritic micro-segregation profiles. EDS line scan analysis for the 1D rod microstructure is shown in Fig. 4.

Fe content changed up to 5 wt% across dendrite arms, while Cr content varied up to 4 wt%. Depressions in the Fe profile correspond to local peaks in the Cr profile, occurring at approximately 6 µm intervals. Enrichment of both Mn (from 1 wt% to 2 wt%) and Mo (1–3 wt%) was observed at the same locations as Cr enrichment (not shown for clarity). The spacing of micro-segregation peaks corresponds with the average 6.5 µm spacing measured for the primary dendrite arms (Table 2), which are indicated by the arrows labeled "PD" in Fig. 4, as expected. Most importantly, the micro-segregation profiles were observed to be regular within the microstructure and did not correlate to any dislocation structures. This demonstrates that the presence of dendrites and chemical inhomogeneity does not necessarily produce dislocations.

Precipitate structures were also analyzed as a potential source of dislocations. Precipitates consisted of either ferrite or oxide precipitates, as indicated by the labels F and P, respectively, in Fig. 3. Ferrite inclusions, identified through t-EBSD crystallographic analysis, typically exhibited irregular morphologies and occurred at grain boundaries (although they were not limited to grain boundaries), and were 500 nm in diameter on average. Oxide precipitates, identified via EDS mapping, were typically Si oxides with Cr and Mn enrichment, exhibited regular spherical morphologies, and were 250 nm in diameter on average. Oxide precipitates were distributed throughout the matrix, and although some were observed near dislocations, there was no evident correlation between the presence of dislocations and precipitate formation.

Orientation image mapping via t-EBSD was used to evaluate whether misorientations inherently exist between most dendrites, and if so, whether these can be linked to dislocation structures. A misorientation map is shown in Fig. 3b for the same area shown in Fig. 3a. In the map, points are colorized according to the relative misorientation of that point with respect to the mean orientation of the grain to which it belongs. Grain boundaries are indicated by thick black lines. Points with a confidence index less than 0.01 were excluded from the analysis and are shown in white as is the background. Ferrite inclusions were removed from the analysis and are shown in white as well, for example as labeled F in Fig. 3b.

Misorientations did not correspond with dendrite structures, instead being distributed throughout the material and concentrated near grain boundaries. Dislocations appeared frequently to be SSDs without notable local misorientation fluctuations, indicating that interdendritic misorientations were not essential to formation of dislocation structures in the 1D DED material. Despite the low dislocation density in the 1D rods, misorientations up to 3 were observed across grains, with the highest local fluctuations near grain boundaries, as shown in the bottom two grains in Fig. 3b. The top grain in Fig. 3b exhibited higher misorientations, but the measurement in the uppermost grain was affected by a much lower foil thickness observed near the top of the foil due to FIB milling. Within the two lower grains, orientation changes were not ob-

Table 4
Dislocation densities [m^{-2}] measured using the line-intercept technique and average dislocation cell size.

	DED			SLM		
	1D	2D	3D	1D	2D	3D
ρ [m^{-2}]	2 x 10^{12}	3 x 10^{13}	1 x 10^{14}	3 x 10^{14}	3 x 10^{14}	4 x 10^{14}
d [nm]	-	-	370	280	400	470

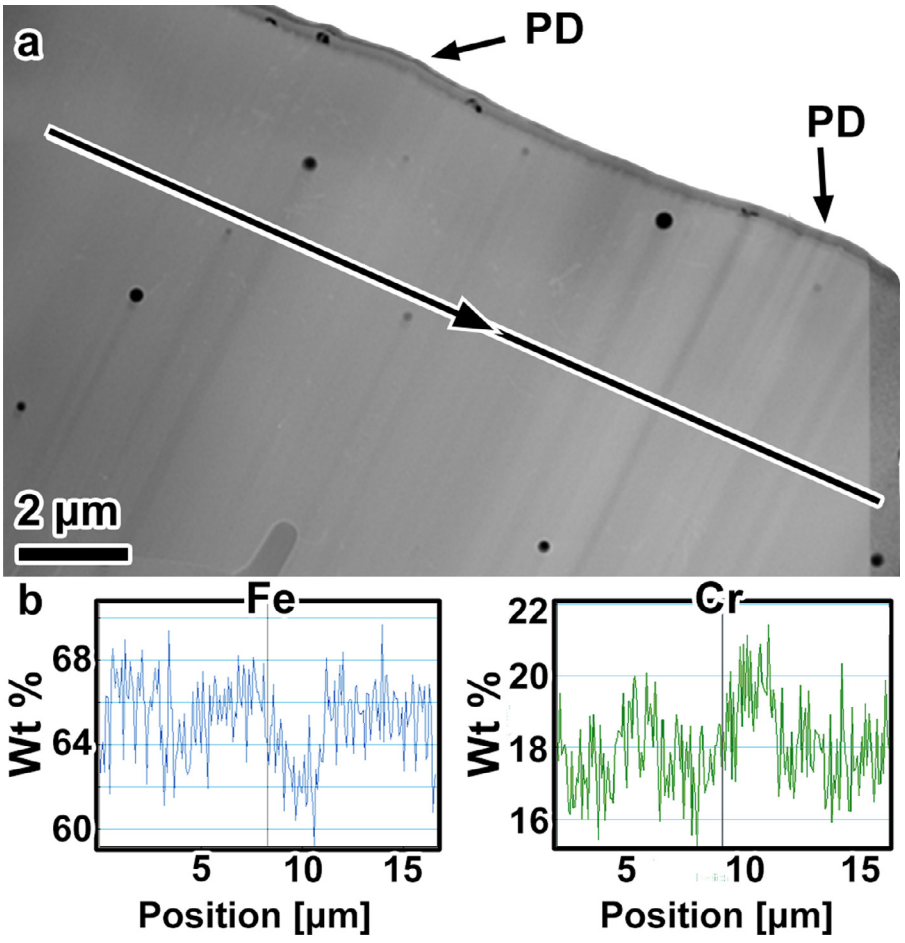

Fig. 4. a. HAADF-STEM of DED 1D rod material, b. EDS data collected from left to right along the line indicated in a. Surface features corresponding to interdendritic micro-segregation labeled PD and indicated by arrows. Color online.

served to occur periodically or correspond to dendrites, indicating that misorientations are not inherent to dendrite structures in the AM material, and that the dislocations present were not inherently tied to any misorientations between dendrites.

3.2.2. DED 2D

The defect microstructure in DED 2D walls exhibited dislocation density an order of magnitude higher than in 1D rods at approximately 3 x 10^{13} m^{-2}, as shown in Fig. 5a. The higher dislocation density coincided with an increased interaction of dislocations, such that they formed pileups at some grain boundaries and dislocation tangles but had not begun to organize into the dislocation walls typical of higher dislocation densities [27]. As in Fig. 3, multiple grains were captured in the extracted region, and are labeled 1–3 in Fig. 5a for clarity.

Primary dendrites were observed corresponding to surface protrusions as indicated by arrows labeled “PD” in Fig. 5a. The PDAS measured at the surface are approximately 6 µm, consistent with the data in Table 2. Most importantly, the PDAS did not coincide with any change in the dislocation density or arrangement, which stayed approximately constant over the measured regions.

EDS analysis was performed along a line perpendicular to the direction of the primary dendrite arms as indicated in Fig. 6. Fe and Cr content fluctuated approximately 5 wt% and 3 wt%, respectively, which is of similar magnitude to that observed in 1D material. Note that micro-segregation occurred over a slightly larger length scale, approximately 9 μm, in the region scanned than the scale of PDAS (average 6 μm) (Table 2). This is attributed to the proximity of a grain boundary to the line scan, which would affect micro-segregation of diffusing species by acting as a sink during cooling after solidification. These observations confirm that a chemically inhomogeneous structure was present with a repeating length scale that was not mirrored in the dislocation structure, which was not periodic or in cells.

Precipitate and ferrite particle structures, labeled P and F respectively in Fig. 5a, were confirmed to have similar composition, size, and distributions as those observed in 1D DED material. In 2D walls, dense tangles of dislocations were observed in the immedi-

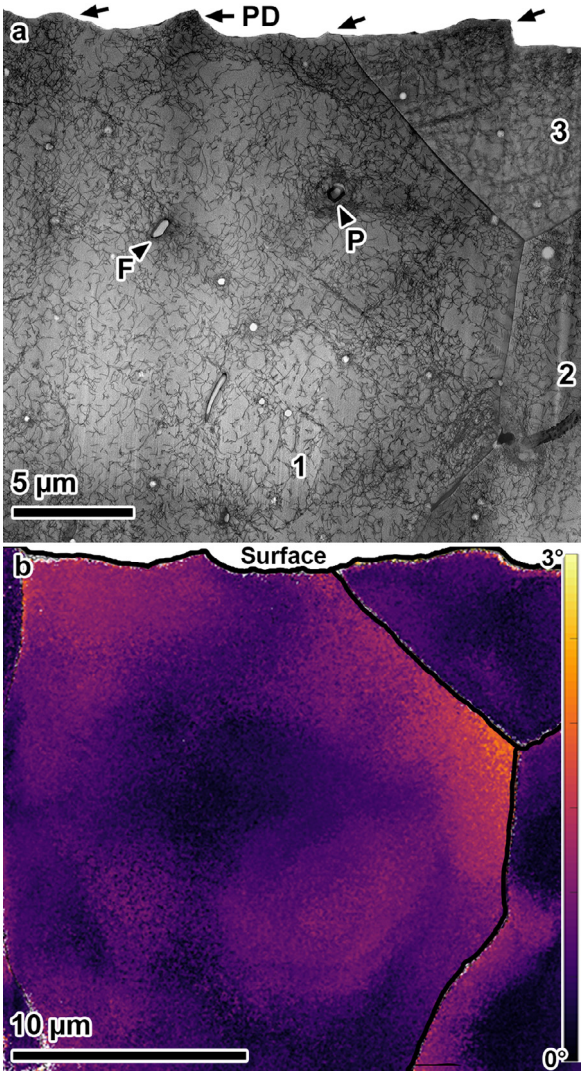

Fig. 5. a. Bright-field zone-axis STEM of microstructures in the DED 2D wall, b. t-EBSD misorientation map of the region shown in a. PD indicates protrusions on the etched surface due to interdendritic micro-segregation, D dislocations, F ferrite inclusions, and P oxide precipitates. Color online.

ately vicinity of most particles (within approximately 100 nm) than in the matrix, for example as shown in Fig. 7 near the precipitates labeled P. However, dislocation pileups, walls, or bands were not observed around the particle structures, such that it remains unclear whether precipitates or dislocations were formed first during microstructural development.

As shown in the orientation map Fig. 5b, intragranular misorientations were limited to less than approximately 3 over a similar area as analyzed in the 1D specimen. Local orientation deviations were not associated with dendrites and were not observed across every dislocation wall or tangle, and locally higher dislocation densities (for example near grain boundaries) were not necessarily associated with misorientations, again indicating that the dislocations were not a product of accommodating differently oriented dendrites.

3.2.3. DED 3D

The DED 3D microstructure was observed directly across the interface with the base plate to compare the deposited, directionally solidified microstructure with that of the pre-annealed base plate, as shown in Fig. 2. The base plate (below the melt pool boundary) experienced nearly the same local thermal and stress-strain history as the adjacent deposit but was not melted and re-solidified. While dendrites were present in the deposited material and not in the base plate, no observable difference in dislocation density was found. Dislocation microstructures across the interface are illustrated in Fig. 8.

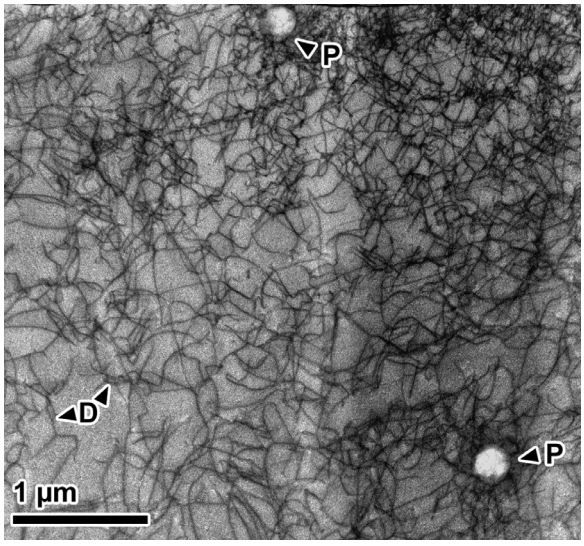

Fig. 6. a. HAADF-STEM image of DED 2D microstructure, b. EDS line scan analysis of micro-segregation profiles, taken from left to right along line indicated in a. Surface protrusion due to etching of interdenritic micro-segregation labeled PD. Color online.

Equiaxed dislocation cells were observed in both the base plate and the deposited material with an average diameter of approximately 370 nm, for example as outlined and labeled C in Fig. 8. These dislocation cells are typical of those observed in SS 316L after deformation [28, 29]. In the deposited 3D prism material and in the base plate, the dislocation density was an order of magnitude higher than in the 2D walls, at approximately 1 x 10^{14} m^{-2}. These density measurements were found to agree with diffraction-based measurements of the dislocation density in similar AM steels [7,13] within an order of magnitude.

While the fine, equiaxed dislocation cells did not change between the base plate and solidified material, a micro-segregation structure was identified in the only deposited material. The micro-segregation appeared as a network with an average diameter of approximately 1.9 μm, corresponding to the PDAS. The dendritic micro-segregation network was superimposed on the dislocation cell structure, and where they overlapped, dislocation walls were thicker and enriched in Cr/depleted in Fe. An example is outlined with the dashed line labeled DCW (for “dendritic cell wall”) in Fig. 8. Examples of the correlation between the thick DCWs and etched, dendritic surface protrusions are arrowed in Fig. 8. Thus, while dislocation cell formation occurred independently of local micro-segregation, there was some overlap between dendrites and wall structures.

Qualitative differences between the cell wall structures with and those without micro-segregation were also observed, indicating different mechanisms of organization. DCWs, outlined with dashed lines in Fig. 9a and shown at higher magnification in Fig. 9b, were not only typically qualitatively wider than other walls, but also contained dislocations that appeared more tangled. In comparison, the regular cell walls had qualitatively more dislocations with straight segments, as shown in Fig. 9c. Tilting of samples in the microscope and observations of grains with different orientations indicated that these differences were general and not due to local projection effects.

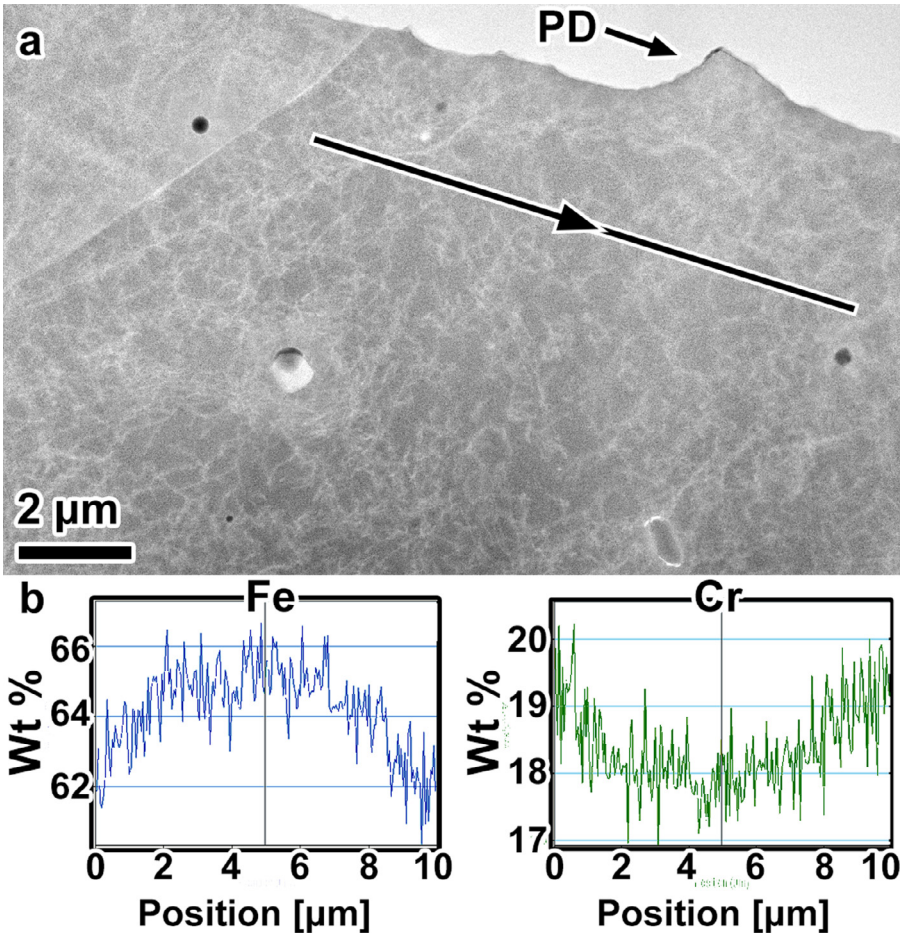

Fig. 7. Bright-field zone-axis STEM of material shown in Fig. 5a illustrating dislocations ("D") organized into tangles and precipitates ("P").

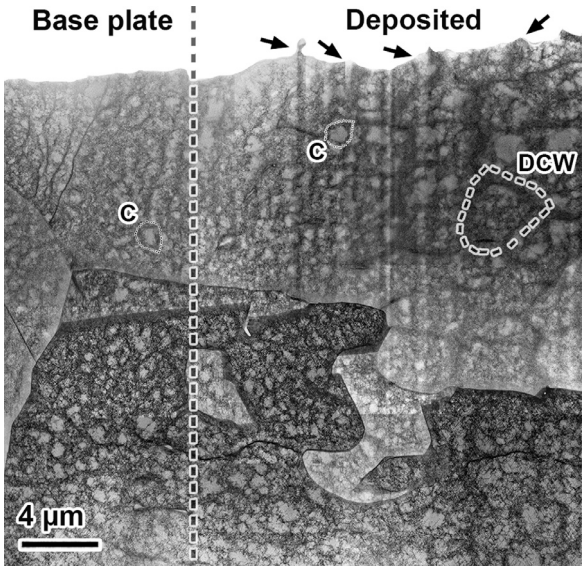

Fig. 8. Bright-field zone-axis STEM imaging of the microstructure across the interface between the as-deposited material of the DED 3D prism and the pre-annealed base plate. The interface is indicated by the dashed line, and surface protrusions due to etching of primary dendrites on the sample surface are indicated with arrows. Examples of dislocation cell walls are outlined, with equiaxed dislocation cells with uniform composition labeled C and cell walls overlapping with dendrite segregation labeled DCW.

Cr and Fe micro-segregation profiles were found to be similar to the Cr micro-segregation profiles observed in the 1D and 2D DED samples, as shown in the EDS maps in Fig 10. Note that EDS and orientation mapping were performed on 3 mm disk specimens instead of the sample extracted via FIB across the interface with the base plate (Fig. 8), as the FIB sample was damaged during handling after S/TEM analysis.

The spacing of the solute-rich regions corresponded to the PDAS, 1.9 μm on average (Table 2), indicating that these were dendrites. While the large, segregated cells frequently appeared equiaxed in images of the thin foils, their matching to the PDAS and solute enrichment supports that they were likely all dendrites elongated in <001> crystallographic directions, as confirmed in some specimens.

Precipitate structures were not limited to dislocation walls, and were not present in all dislocation walls, indicating a lack of correlation between precipitation of second phases and dislocation wall formation. Precipitates exhibited similar size, composition, and distribution as those in the 1D and 2D components. Although many were found in the solute-rich large cell walls, they were also observed in the walls of the smaller cells with uniform composition and within the cell interiors. Ferrite was observed in the solidified DED material near the base plate, but no ferrite was observed in the DED 3D material a few mm away from the base plate.

In the 3D DED material, misorientations between DCWs were found not to be a requirement for dislocation cell wall formation. Orientation mapping was performed near the edge of a 3 mm TEM disk, as shown in Fig. 11. Three grains, with grain boundaries indicated by black lines, were captured in the map near the edge

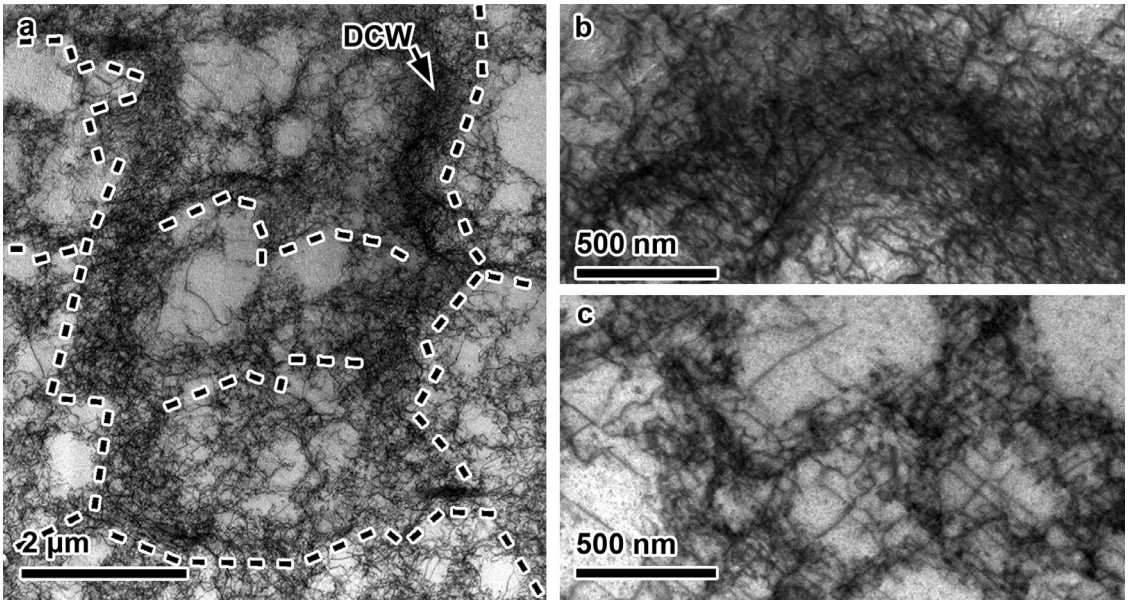

Fig. 9. Bright-field zone-axis STEM images of dislocation structures in as-deposited DED 3D rectangular prisms. a. Dislocation cell walls with micro-segregation (DCW, dashed lines and arrow) and uniform-composition cells, b. DCW, c. walls of equiaxed cells with uniform composition.

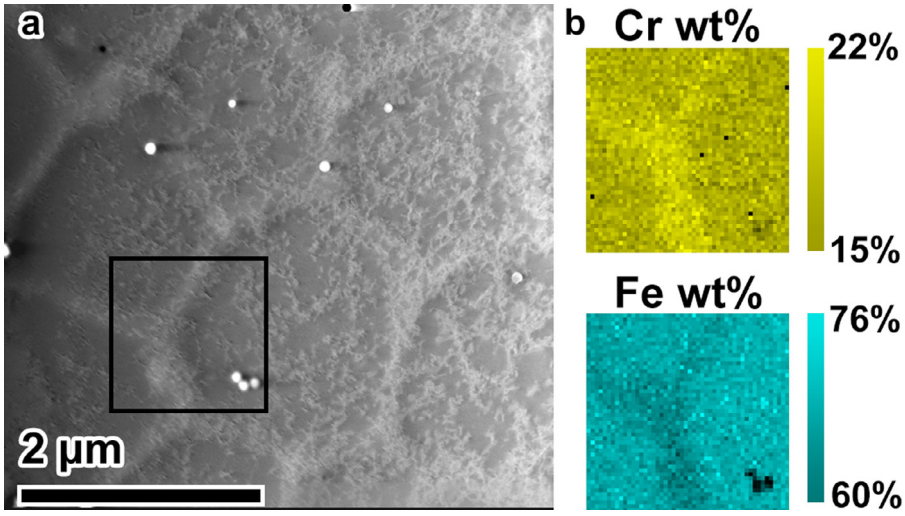

Fig. 10. a. HAADF-STEM image and b. EDS mapping of the boxed region in a, illustrating Cr micro-segregation and Fe depletion at large dislocation cell walls. Color online.

of electropolished hole, which appears at the bottom right. Large dendritic cells were observed via TEM and were visible in the image quality analysis of the mapped region. The DCWs were traced in the image quality map, then overlaid on the misorientation map to reveal any correlation between DCWs and local orientation deviations. Misorientations up to 5 were observed over a range of approximately 20 μm, and tended to be highest near grain boundaries, as shown in Fig. 11. Local orientation deviations were not observed across the majority of the dendritic dislocation cell walls, although some correlations occurred, for example near the arrow in Fig. 11.

3.3. SLM microstructures

3.3.1. Thermal constraints

In SLM parts, the melt pool penetration of the substrate and the time required to spread new powder layers between layers were both greater than in DED parts. These differences changed the solidification behavior such that even in the SLM 1D rods, thermal contraction was not unconstrained as it was in DED 1D rods. In SLM materials, the melt pool appeared to penetrate up to 200 μm into the substrate, while layers were built in 20 μm increments. For example, analysis of the top of the SLM 1D rods (where the approximate shape of the deposit was preserved for the final layer) indicated that melt pools were up to 180 µm deep, as shown in Fig. 2g by the line labeled as the layer boundary. The melt pool profile typically extended up to 100 µm deeper in the center of the part than at the edges, suggesting that the deposited material was surrounded and constrained by the substrate upon solidification. Similar penetration of the substrate by new layers was observed for SLM 2D walls and 3D components, confirming that the deposited material was constrained in all SLM parts. Despite the presence of these constraints, the volume of substrate material surrounding the melt pool should have been smallest in 1D rods, larger in 2D walls, and largest in 3D prism. Correspondingly, the *magnitude* of the constraints was still expected to increase with increasing part dimension in SLM parts.

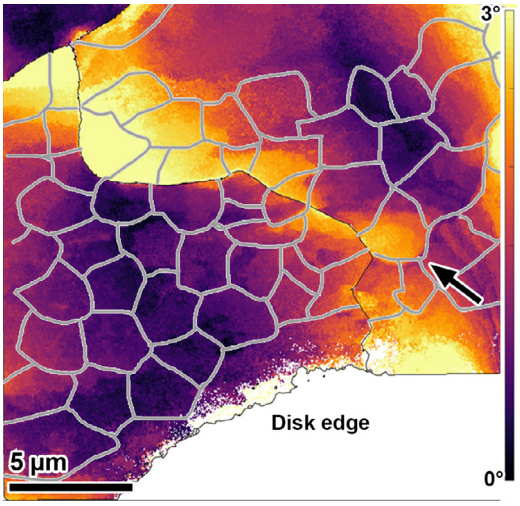

Fig. 11. Map of misorientation relative to the grain mean orientation for a 3 mm disk prepared from the DED 3D rectangular prism, with approximate locations of dislocation cells traced in gray. Each point colorized according to the color bar shown at the right. Color online.

3.3.2. Dislocation microstructures

The microstructure of the SLM materials differed from the DED materials in terms of scale, density, and organization. Dislocation densities ranged from 3–4 x 10^{14} m^{-2} in SLM materials, as listed in Table 4. Defect microstructures in SLM material showed organization into cells elongated on {001}-type crystallographic planes (instead of equiaxed cells), as shown in Fig. 12 for a. 1D, b. 2D, and c. 3D components. The average cell sizes were 280 nm, 400 nm, and 470 nm in 1D, 2D, and 3D SLM parts, respectively (Table 4). These average dislocation cell sizes matched the PDAS observed on the etched surfaces, which were 270 nm, 390 nm, and 460 nm in 1D, 2D, and 3D material, respectively (Table 2).

SEM imaging during FIB milling of etched surfaces and S/TEM imaging after extraction of TEM lamellae revealed coincidence of dislocation cells with dendritic micro-segregation patterns in SLM specimens. Dislocation cells have been frequently reported to overlap with dendritic micro-segregation profiles with spacing 400–600 nm for SLM SS 316L [5,6,10,18,30–32]. Consequently, EDS analysis was not considered necessary to verify that dislocation cells overlapped with dendrites in SLM specimens, although additional EDS analysis is being pursued in ongoing studies.

1D SLM dislocation structures are shown in the edge-on orientation in Fig. 12a, with the end-on orientation shown at higher magnification in the inset.

In the 1D SLM material, dislocation cell walls were organized loosely, with substantial dislocation density between the cells, in contrast to the more densely packed cell structures typically reported for SLM SS 316L [6]. Although dislocations were organized sufficiently such that cell walls could be delineated from the interiors, discrete dislocations could frequently still be discerned within the cell walls, Fig. 12a inset. Line-intercept measurements indicated an approximate dislocation density of 3 x 10^{14} m^{-2}, which represents a slight increase relative to DED 3D parts but is within the same order of magnitude.

In SLM 2D parts, shown in Fig. 12b, dislocation cells were only observed in the end-on orientation due to the sample orientation. The cell structures were approximately 400 nm in diameter on average, slightly higher than in 1D SLM parts, and the cell walls appeared denser and tighter than in 1D material. Dislocation density was approximately the same as in SLM 1D parts at approximately 3 x 10^{14} m^{-2}.

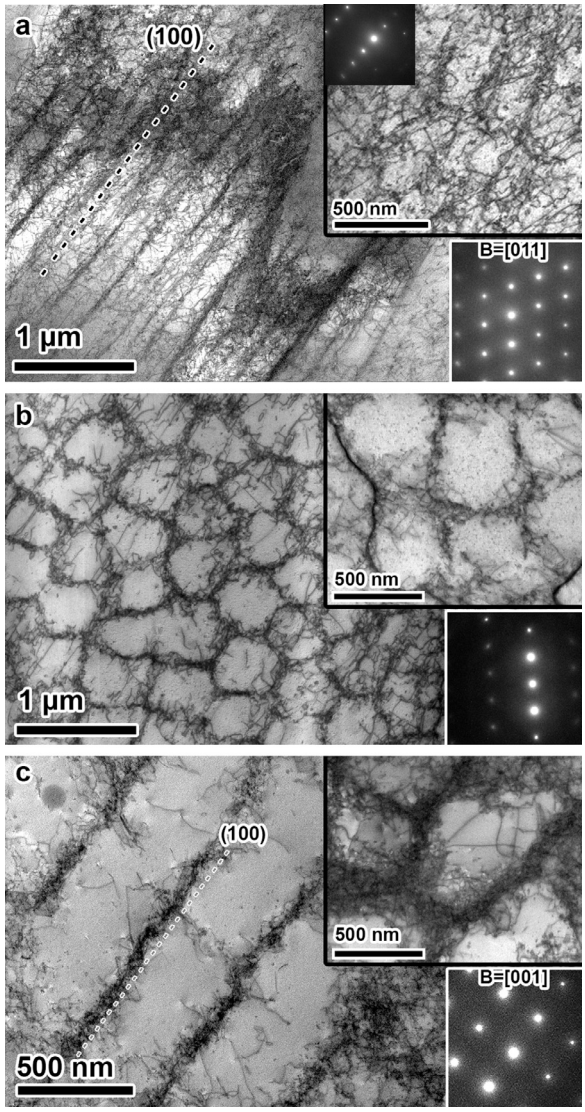

Fig. 12. Bright-field STEM images of dislocation structures in a. SLM 1D rods viewed edge-on, with end-on view inset; b. SLM 2D wall material viewed end-on; and c. 3D material viewed edge-on, with end-on view inset.

In 3D SLM parts, shown in Fig. 12c, dislocation cells were largest at approximately 470 nm average diameter, similar to other observations in SLM SS 316L parts [5,6,10,18]. The elongated, periodic structures shown in the edge-on orientation in Fig. 12c, indicated parallel to the dashed lines, were observed to extend throughout all grains. Qualitatively, dislocation walls were denser than those observed in SLM 1D rods, such that individual dislocations were unable to be delineated within walls. The estimated dislocation density was 4 x 10^{14} m^{-2}, which is in agreement with reports in the literature [13].

3.3.3. Precipitates

Fine precipitates approximately 15 nm in diameter on average were present in all SLM specimens, primarily in cell walls but also in cell interiors. These were confirmed for SLM 3D structures to be Si, Mn, and Cr oxides, as reported in other studies of SLM 316L [6,33]. No differences were observed in the precipitate composition, average size, or distribution for SLM 1D-3D parts. Here, oxides were primarily observed within cell walls, although some were found within cell interiors as well. No ferrite was observed.

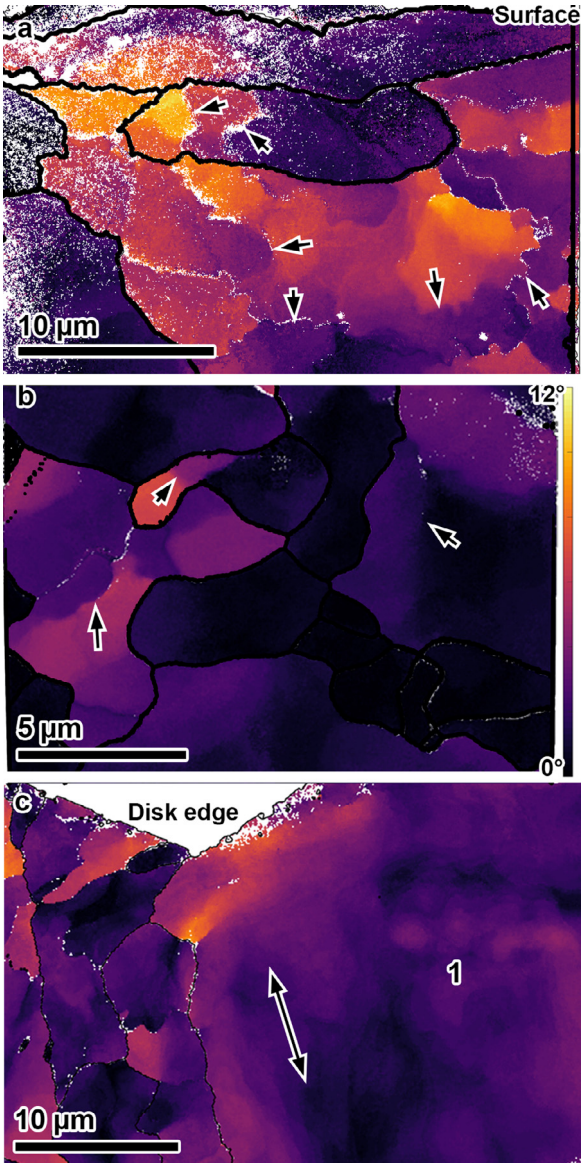

Fig. 13. Maps of the misorientation of each point relative to the grain mean orientation collected from transmission EBSD data for a. SLM 1D rods, b. SLM 2D walls, and c. SLM 3D material. Note different spatial scales in a, b, and c. Color online.

3.3.4. Misorientations

Orientation mapping of SLM materials indicated that in general, larger orientation gradients developed in SLM parts compared to DED, as shown in the orientation maps in Fig. 13 (note the different scale than in the DED misorientation maps). However, orientation gradients were once again not present across most cell walls, indicating that local misorientations are not required to form the cell walls.

In SLM 1D and 2D materials, dislocation cells were observed via TEM across the entire regions shown in Fig. 13a and b, but local misorientations were observed only across of fraction of these cell walls, for example as shown near the arrows in Fig. 13a and b. In the SLM 3D material, misorientations followed similar patterns, Fig. 13c. In the large grain labeled 1 in Fig. 13c, dislocation cells were observed in TEM to be in an edge-on orientation across the entire grain, along the direction indicated by the arrow. It is clear in Fig. 13 that orientation deviations occurred in random patterns and not across the elongated, straight cell structures.

4. Discussion

4.1. Summary of microstructural observations

The most important observations made in this study were as follows.

1 Dislocation density increased with increasing constraints around the melt pool.
   a Density increased by an order of magnitude with each increase in part dimension in DED parts.
   b In SLM parts, dislocation density and organization in cell walls increased qualitatively with increasing part dimensionality.
2 Dendrites were observed in all specimens.
   a Dendrites existed without overlapping dislocation structures in DED 1D and 2D parts.
   b In DED 3D parts, dendrites overlapped some dislocation cell walls, but many dislocation cell walls with uniform composition existed between the dendrites.
   c In SLM parts, dislocation structures exhibited the same spacing and orientation as dendrites, and spacing increased with increasing part dimensionality.
3 Precipitates were not correlated with the location of dislocation wall formation, and precipitate density was not correlated with dislocation density.
4 Misorientations were not observed across all dislocation walls in all components. Misorientations were not observed across all dendrites. Thus, neither the formation of dendrites nor the formation of dislocation walls was inherently tied to the presence of a local misorientation.

In the following, the results are shown to support the hypothesis that thermal shrinkage and expansion in a constrained medium are the primary sources for the dislocations observed in AM parts. In other words, the dislocation density and structure are determined by the residual stresses and strains developed after solidification. The studied solidification microstructural features investigated, specifically dendrites, precipitate networks, and misorientations between dendrites, did not produce substantial dislocation density independently of thermal stress/strain. The influence of these solidification features was to affect the organization of dislocations later in the process, after dislocations were produced by the thermal cycling.

4.2. Geometrical constraints and micro-segregation

4.2.1. DED

The increase in constraints from 1D to 2D to 3D DED parts led to an increase in dislocation density from 10^{12} m^{-2} to 10^{13} m^{-2} to 10^{14} m^{-2}, respectively, indicating a correlation between dimensionality/constraints and deformation microstructure. Defect microstructures are depicted schematically in Fig. 14, where the dendrite growth direction (GD) is vertical from bottom to top, interdendritic regions exhibiting micro-segregation are shown in green (for example “ID segregation” in Fig. 14a), and individual dislocations are shown in black.

1D DED microstructures showed that in the absence of constraints to thermal contraction after solidification, dislocation density is minimal. This material showed that dendrites can exist without being accommodated by dislocations, so any coherency stresses induced by compositional changes are alone insufficient to nucleate enough dislocations to begin interacting or organizing into walls. The 1D microstructure is depicted in Fig. 14a, with discrete, sparse dislocations shown in black distributed throughout the matrix and the ID regions.

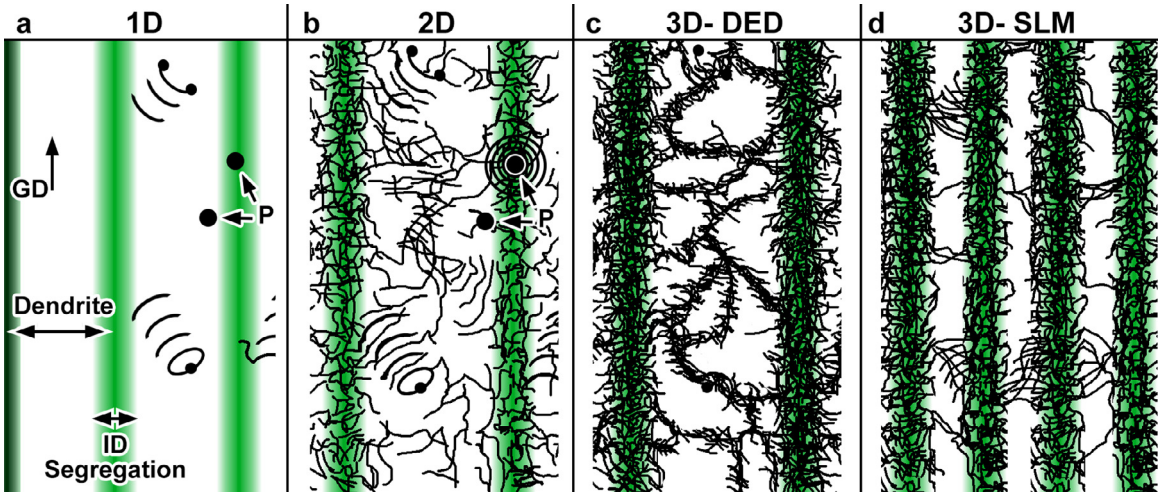

Fig. 14. Schematic illustrating dendrite (green) and dislocation (black) structures in a. 1D, b. 2D, and c, d. 3D materials. Solidification/dendrite growth direction indicated from bottom to top. Precipitates labeled "P", growth direction "GD" is vertical. Color online.

In the 2D DED case, dislocation density increased by an order of magnitude with the introduction of constraints in the build direction, as shown schematically in Fig. 14b. This indicates that the dislocation density is directly tied to the geometric constraints to thermal volume changes. The lack of increased organization around dendritic patterns further confirms that the ability of dendrites to produce and trap dislocations is alone insufficient to create organized dislocation cell structures.

In 3D DED parts, dislocation density increased by another order of magnitude, becoming high enough to create dense, organized dislocation cell walls similar to those typically formed under tensile, compressive, or torsional loading [34–36]. These structures are depicted in Fig. 14c. The adjacent material in the base plate exhibited similar dislocation density and dislocation structures, despite the lack of a solidification structure. Since the deposit and adjacent base plate material share only thermal history and similar strains, but not the directional solidification features, this confirms that the density and length scale of AM dislocation structures are primarily determined by stress/strain history.

Dendrite micro-segregation appeared to have a minimal influence, and only on dislocation walls that directly overlapped them. DCWs appeared to be thick and comprised primarily tangled dislocation segments, while dislocation cell walls without micro-segregation formed between and subdividing dendrites with more straight dislocation segments, as depicted in Fig. 14c. This indicates that the interdendritic regions with micro-segregation are not always the most energetically favorable place for dislocations to organize. Consequently, it can be concluded that dislocation cell formation tends to follow patterns observed in conventional materials, except for walls that form in the immediate vicinity of dendrites.

Birnbaum et al. [18] suggested that chemical micro-segregation to dislocation walls in AM materials is driven by strain aging occurring *after* dislocation structure formation. The presence of dendrites without dislocations in the 1D DED material in this study confirms that the micro-segregation occurs early in the process during solidification, as dendrites typically form, and is not based on dislocations acting as sinks for segregants. In the 3D DED material, the presence of micro-segregation only at some dislocation walls further validates that the micro-segregation is not a general or post-solidification phenomenon. Finally, the micro-segregation patterns fall on {001} crystal planes, which is expected for dendrites in cubic materials, and which is not typical of dislocation structures in FCC metals deformed conventionally from room temperature to approximately 600 °C [28,29,37,38].

4.2.2. SLM

Although it was not possible to minimize constraints in 1D or 2D SLM parts as effectively as in DED parts, the magnitude of constraints was still expected to be different between 1D, 2D, and 3D SLM parts. This hypothesis was supported by observations that the organization of dislocation walls was qualitatively different between 1D, 2D, and 3D SLM parts, similar to observations made in DED materials. Thus, the geometric constraints and residual stresses and strains still had an influence on the dislocation structures.

Unlike in 3D DED material, dislocation walls in SLM materials overlapped directly with primary dendrites, as depicted in Fig. 14d. The dislocation cell size also increased from 1D-3D in SLM materials, even though the dislocation density stayed within the same range or slightly increased from 1D-3D. This could be interpreted as an increased importance of dendrites in SLM materials compared to DED. However, the greater correlation between dendrite arms and dislocation cells in SLM parts can be attributed to how much closer the dendrite spacing was to the dislocation cell size as follows.

In the 316L base plate with no solidification features that the 3D DED prism was printed on, a dislocation density on the order of 10^{14} m^{-2} corresponded to a dislocation cell diameter of 370 nm on average. In conventional materials, dislocation cell size is inversely related to dislocation density after deformation, with established relationships that depend on the alloy and composition [27,39,40]. The SLM and DED specimens had similar compositions (Table 1), indicating that they should exhibit similar cell sizes at similar dislocation densities. For the SLM materials with dislocation density slightly higher than in the 316L base plate but still on the order of 10^{14} m^{-2}, dislocation cells would therefore be estimated to be slightly smaller size on average than 370 nm. In all SLM parts, the PDAS fell within +/-25% of the predicted average dislocation cell size of less than 370 nm. In the 3D DED part, the PDAS was approximately 500% of the 370 nm average dislocation cell size. Since it appears favorable for dislocation walls in close proximity of dendrites to organize aligned with the dendrite micro-segregation, as shown in Figs. 8 and 9, then it follows that if dendrite walls would be within close proximity to all dislocation walls, they would naturally interact and overlap. Consequently, there would be more op-

portunity to form dislocation walls between/subdividing dendrites in DED material than in SLM.

While the magnitude of micro-segregation was not quantified in SLM material relative to that observed in DED material, it is considered unlikely that differences in the magnitude of micro-segregation drove the differences between SLM and DED dislocation structures. Greater micro-segregation of the same elements or different segregating species, particularly elements with greater atomic mismatch relative to Fe, could be posited to increase constitutional stresses due to solute segregation in SLM 316L, creating more dislocations and greater dislocation trapping at dendrites [8]. However, SLM materials have been shown to exhibit a dislocation structure with all cells aligned with dendrites even in the presence of relatively low amounts of micro-segregation of elements including Cr and Mo [6,8]. This supports the notion that high levels of chemical micro-segregation are not necessary to cause overlap of dislocation cells with dendrites. Therefore, the presence of dislocation walls overlapping with dendrites is primarily driven by the degree of difference between the PDAS and the preferred dislocation cell size for the observed density.

4.3. Precipitate networks

The results support the notion that precipitate networks were not critical to dislocation production or organization, and they have at most an ancillary influence on the development of AM dislocation structures.

4.4. Misorientations between solidifying dendrites

Orientation differences between dendrites at solidification were not found to be sufficient to form boundaries composed largely of GNDs. Classically, dislocation structures in metals can be classified in one of two categories, either GNDs or statistically stored dislocations (SSDs). GNDs are accompanied by local lattice rotations and accommodate local shape or orientation changes, while SSDs do not [36,41–44]. If misorientations between dendrite arms were large enough to warrant accommodation by dislocations, these dislocations would necessarily be GNDs.

Orientation mapping of DED 1D and 2D parts indicated that in material with dendrites but not dislocation cells, local misorientations did not accompany dendrite arms, as shown in Figs. 3 and 5. This indicates that dendrites are not inherently misoriented relative to one another, and their presence does not necessarily produce GNDs. 3D DED and all SLM parts showed that in material with both dendrites and dislocation cell structures, local misorientations still did not generally accompany dendrites, as shown in Figs. 11 and 13. Thus, even when dislocation walls coincided dendrites, they did not necessarily comprise GNDs, indicating that GNDs and local misorientations are not critical to the formation of AM dislocation structures.

While the misorientations across cell walls were only observed post mortem and not during the initial stages of formation, the misorientation across a cell wall only tends to increase with increasing strain/deformation [36]. Thus, it is considered unlikely that misorientations were present across all dendrite walls during formation that were not observed post mortem. The results do not preclude the possibility that misorientations between dendrites may be accommodated by GNDs, or that these GNDs could influence some dislocation structures. The evidence simply indicates that misorientations are neither the primary element causing nucleation of dislocations nor the most influential factor in dislocation structure organization.

The observation that lattice misorientations increase with geometric constraints, and thus thermal stresses, is supported by additional larger-scale analysis of grain average misorientations and kernel average misorientations (KAM) obtained via EBSD analysis of the surfaces of bulk samples, shown in Supplemental Fig. 1 and 2. Generally, an increase in the average degree of misorientation and the KAM was observed with increasing geometric constraints. Studies investigating the correlations between these surface orientation analyses and dislocation structures are ongoing.

4.5. Linking processing parameters and dislocation structures

If stresses and strains induced by thermal distortions dictate the dislocation density, and solidification microstructures (particularly primary dendrite arms) influence the dislocation organization, it is important to develop methods to control thermal distortions and solidification features. Thermal distortions/residual stresses and dendrite structures have been shown to be influenced by thermal gradients, cooling rate during solidification, and number of thermal cycles [5,45,46], all of which can be controlled by manipulating AM processing parameters.

Cooling rate influences thermal distortions by setting the effective strain rate, since it would determine the time in which the volume shrinks, and by influencing local temperature and strain gradients. Cooling rate may be increased by increasing the volume of cooler substrate material surrounding the deposited hot melt pool, or by decreasing the temperature of the substrate relative to the melt. An increased volume of substrate relative to melt pool size was achieved in the current study as dimensions were increased from 1D to 3D. Part to melt pool volume ratio was also increased from DED to SLM for 3D parts, since 3D parts were similarly sized but the laser spot size was 600 μm in DED and 100 μm in SLM. In both situations an increase in dislocation density was observed. Cooling rate and thermal gradients were also increased in SLM relative to DED due to a lower substrate temperature in SLM, which occurred since the time between layers was longer in SLM to allow for recoating compared to the continuous deposition with DED.

Cooling rate during solidification also influences dendrite spacing, with higher cooling rates leading to smaller spacing (especially of secondary dendrite arms) [19]. Increasing dendrite size has been shown to effectively increase the dislocation cell spacing in SLM 316L SS [5].

Thermal gradients control how localized thermal distortions are around the melt pool, and thus control strain localization. Higher strain localization would result in accommodation by locally higher dislocation densities, which, when produced throughout a part, would induce overall higher dislocation densities. Higher thermal gradients in SLM parts corresponded to higher dislocation densities compared to DED parts in this work. However, thermal gradient and cooling rate are directly related, so the sole influence of thermal gradient could not be discerned in this study, requiring additional work varying thermal gradients while keeping cooling rates constant.

Finally, the number of heating and cooling cycles or laser scan passes within a layer can be expected to influence the dislocation density. If dislocations are induced each time material is heated by close proximity to the melt pool and subsequently cooled down, then increasing the number of cycles would increase the final density. It has been shown that decreasing the layer height, and thereby increasing the number of layers, increases distortion while reducing residual stresses [46]. Since layers are smaller in SLM than in DED parts, a part of the same size experiences significantly more heating/cooling cycles in SLM, which would partially explain the differences observed in DED and SLM dislocation density. Additionally, DED parts experienced an increasing number of heating and cooling cycles with increasing dimensionality, starting from 1D rods which experienced no repeated cycling.

During cooling from freezing temperature (approximately 1400°C) to room temperature in SS 316L, thermal contraction can amount to local strains of up to 1.7% [17]. Dislocation densities measured in SLM 316L both in this study, Table 4, and in other works, have indicated densities on the order of 10^{14}–10^{15} m^{-2} in3D components, which is close to that observed at 20% cold work [4,13,47]. However, even single tracks of material deposited by AM have exhibited cellular dislocation structures without thermal cycling [8]. Thus, thermal cycling is not considered to be a requirement for development of a dislocation structure, but represents a viable method to increase dislocation density if desired.

In conclusion, the results of this study suggest that controlling print parameters to manipulate cooling rate, thermal gradient, and number of passes/hatch spacing or number of layers would provide a viable means to control the dislocation structures in AM 316L SS, and ultimately the mechanical properties.

5. Conclusions

This study is the first to reveal the origin of dislocation structures in AM SS 316L by systematically manipulating thermal stresses in AM components by altering the geometric constraints on the fabricated samples. The results indicated the following:

1 The primary source of dislocations in AM materials is deformation induced by thermal expansion/shrinkage in a constrained medium.
2 Dendritic micro-segregation influences dislocation structure orientation and scale if the average primary dendrite arm spacing is close to the average dislocation cell size that would form for the observed dislocation density.
3 Constitutional stresses due to micro-segregation, coherency strains due to precipitation networks, and misorientations between dendrites are not the sources of dislocation structures in AM 316L SS.
4 Features that can be controlled by manipulating processing parameters to influence dislocation structure development and density include:
   a Cooling rate. This determines the spacing of dendrite arms, which act as obstacles to dislocation motion, as well as the effective strain rate during cooling.
   b Thermal gradient. This determines the localization of the stresses and strains.
   c Hatch and layer spacing. These determine the number of heating and cooling cycles, which determines the number of times a part is distorted locally and the amount of accumulated strain that is accommodated by dislocations.
   d Melt pool penetration of the substrate. This determines the direction and magnitude of geometric constraints that are present around newly deposited material during shrinkage.

The relationships outlined above give several potential means of controlling the dislocation microstructure in AM materials to further improve properties and mechanical response.

Declaration of competing interest

The authors declare that they have no known competing financial interests or personal relationships that could have appeared to influence the work reported in this paper.

Acknowledgements

The electron microscopy was carried out using facilities and instrumentation that are partially supported by the National Science Foundation (NSF) through the Materials Research Science and Engineering Center (DMR-1720415). The authors would like to acknowledge further support from the Department of Energy / National Nuclear Security Administration under Award Number DE-NA0003921, the NSF-DMREF through the grant DMR-1728933, and NSF through the grant CMMI-1561899. Authors would also like to thank the Grainger Institute for Engineering for seeding this research activity. The EOS M290 was supported with UW2020 WARF Discovery Institute funds. KMB gratefully acknowledges support from Lawrence Livermore National Laboratory; Lawrence Livermore National Laboratory is operated by Lawrence Livermore National Security, LLC, for the U.S. Department of Energy, National Nuclear Security Administration under Contract DE-AC52-07NA27344. Disclaimer: This report was prepared as an account of work sponsored by an agency of the United States Government. Neither the United States Government nor any agency thereof, nor any of their employees, makes any warranty, express or implied, or assumes any legal liability or responsibility for the accuracy, completeness, or usefulness of any information, apparatus, product, or process disclosed, or represents that its use would not infringe privately owned rights. Reference herein to any specific commercial product, process, or service by trade name, trademark, manufacturer, or otherwise does not necessarily constitute or imply its endorsement, recommendation, or favoring by the United States Government or any agency thereof. The views and opinions of authors expressed herein do not necessarily state or reflect those of the United States Government or any agency thereof.

Supplementary materials

Supplementary material associated with this article can be found, in the online version, at doi:10.1016/j.actamat.2020.07.063.

References

[1] T. DebRoy, H.L. Wei, J.S. Zuback, T. Mukherjee, J.W. Elmer, J.O. Milewski, A.M. Beese, A. Wilson-Heid, A. De, W. Zhang, Additive manufacturing of metallic components – Process, structure and properties, Prog. Mater Sci. 92 (2018) 112–224 https://doi.org/10.1016/j.pmatsci.2017.10.001.
[2] W.E. Frazier, Metal Additive Manufacturing: A Review, J. Mater. Eng. Perform. 23 (6) (2014) 1917–1928 https://doi.org/10.1007/s11665-014-0958-z.
[3] D. Herzog, V. Seyda, E. Wycisk, C. Emmelmann, Additive manufacturing of metals, Acta Mater 117 (2016) 371–392 https://doi.org/10.1016/j.actamat.2016.07.019.
[4] M. Shamsujjoha, S.R. Agnew, J.M. Fitz-Gerald, W.R. Moore, T.A. Newman, High strength and ductility of additively manufactured 316L stainless steel explained, Metall. Mater. Trans. A 49 (7) (2018) 3011–3027 https://doi.org/10.1007/s11661-018-4607-2.
[5] L. Liu, Q. Ding, Y. Zhong, J. Zou, J. Wu, Y.-L. Chiu, J. Li, Z. Zhang, Q. Yu, Z. Shen, Dislocation network in additive manufactured steel breaks strength–ductility trade-off, Mater. Today 21 (4) (2018) 354–361 https://doi.org/10.1016/j.mattod.2017.11.004.
[6] Y.M. Wang, T. Voisin, J.T. McKeown, J. Ye, N.P. Calta, Z. Li, Z. Zeng, Y. Zhang, W. Chen, T.T. Roehling, R.T. Ott, M.K. Santala, Philip J. Depond, M.J. Matthews, A.V. Hamza, T. Zhu, Additively manufactured hierarchical stainless steels with high strength and ductility, Nat. Mater. 17 (2017) 63 https://doi.org/10.1038/nmat5021.
[7] C.A. Bronkhorst, J.R. Mayeur, V. Livescu, R. Pokharel, D.W. Brown, G.T. Gray, Structural representation of additively manufactured 316L austenitic stainless steel, Int. J. Plast. 118 (2019) 70–86 https://doi.org/10.1016/j.ijplas.2019.01.012.
[8] K. Saeidi, X. Gao, Y. Zhong, Z.J. Shen, Hardened austenite steel with columnar sub-grain structure formed by laser melting, Mater. Sci. Eng. A 625 (2015) 221–229 https://doi.org/10.1016/j.msea.2014.12.018.
[9] Y. Zhong, L. Liu, S. Wikman, D. Cui, Z. Shen, Intragranular cellular segregation network structure strengthening 316L stainless steel prepared by selective laser melting, J, Nucl. Mater. 470 (2016) 170–178 https://doi.org/10.1016/j.jnucmat.2015.12.034.
[10] Z. Sun, X. Tan, S.B. Tor, W.Y. Yeong, Selective laser melting of stainless steel 316L with low porosity and high build rates, Mater. Des 104 (2016) 197–204 https://doi.org/10.1016/j.matdes.2016.05.035.
[11] A. Rukwied, A.W. Ruff, W.A. Willard, Study of the cellular solidification structure in a continuously cast high purity copper, Metall. Mater. Trans. B 2 (8) (1971) 2105–2114 https://doi.org/10.1007/bf02917538.
[12] D.W. Brown, D.P. Adams, L. Balogh, J.S. Carpenter, B. Clausen, G. King, B. Reedlunn, T.A. Palmer, M.C. Maguire, S.C. Vogel, In situ neutron diffraction study of the influence of microstructure on the mechanical response of additively manufactured 304L stainless steel, Metall. Mater. Trans. A 48 (12) (2017) 6055–6069 https://doi.org/10.1007/s11661-017-4330-4.

[13] R. Pokharel, L. Balogh, D.W. Brown, B. Clausen, G.T. Gray, V. Livescu, S.C. Vogel, S. Takajo, Signatures of the unique microstructure of additively manufactured steel observed via diffraction, Scripta Mater 155 (2018) 16–20 https://doi.org/10.1016/j.scriptamat.2018.06.008.
[14] D.A. Ramirez, L.E. Murr, E. Martinez, D.H. Hernandez, J.L. Martinez, B.I. Machado, F. Medina, P. Frigola, R.B. Wicker, Novel precipitate–microstructural architecture developed in the fabrication of solid copper components by additive manufacturing using electron beam melting, Acta Mater 59 (10) (2011) 4088–4099 https://doi.org/10.1016/j.actamat.2011.03.033.
[15] Y.S.J. Yoo, T.A. Book, M.D. Sangid, J. Kacher, Identifying strain localization and dislocation processes in fatigued Inconel 718 manufactured from selective laser melting, Mater. Sci. Eng. A 724 (2018) 444–451 https://doi.org/10.1016/j.msea.2018.03.127.
[16] B. Barkia, P. Aubry, P. Haghi-Ashtiani, T. Auger, L. Gosmain, F. Schuster, H. Maskrot, On the origin of the high tensile strength and ductility of additively manufactured 316L stainless steel: Multiscale investigation, J, Mater. Sci. Technol. 41 (2020) 209–218 https://doi.org/10.1016/j.jmst.2019.09.017.
[17] S. Gorsse, C. Hutchinson, M. Gouné, R. Banerjee, Additive manufacturing of metals: a brief review of the characteristic microstructures and properties of steels, Ti-6Al-4V and high-entropy alloys, Sci. Technol. Adv. Mat. 18 (1) (2017) 584–610, doi:10.1080/14686996.2017.1361305.
[18] A.J. Birnbaum, J.C. Steuben, E.J. Barrick, A.P. Iliopoulos, J.G. Michopoulos, Intrinsic strain aging, Σ3 boundaries, and origins of cellular substructure in additively manufactured 316L, Addit. Manuf. 29 (2019) 100784 https://doi.org/10.1016/j.addma.2019.100784.
[19] W. Kurz, D.J. Fisher, „ Fundamentals of solidification, Trans Tech Publications, Aedermannsdorf, Switzerland, 1986.
[20] F. Bachmann, R. Hielscher, H. Schaeben, Grain detection from 2d and 3d EBSD data—Specification of the MTEX algorithm, Ultramicroscopy 111 (12) (2011) 1720–1733 https://doi.org/10.1016/j.ultramic.2011.08.002.
[21] D.A. Porter, K.E. Easterling, Phase transformations in metals and alloys Van Nostrand Reinhold, New York, 1981.
[22] J.W. Elmer, S.M. Allen, T.W. Eagar, Microstructural development during solidification of stainless steel alloys, Metall. Trans. A 20 (10) (1989) 2117–2131 https://doi.org/10.1007/bf02650298.
[23] D.J. Thoma, G.K. Lewis, R.B. Nemec, Solidification behavior during directed light fabrication, Los Alamos National Laboratory, 1995.
[24] D.J.C. Thoma, Lewis, G.K. & Nemec, R.B. , Directed light fabrication of iron-based materials, Los Alamos National Laboratory, 1995.
[25] D.M. Norfleet, D.M. Dimiduk, S.J. Polasik, M.D. Uchic, M.J. Mills, Dislocation structures and their relationship to strength in deformed nickel microcrystals, Acta Mater. 56 (13) (2008) 2988–3001 https://doi.org/10.1016/j.actamat.2008.02.046.
[26] P.B. Hirsch, Electron microscopy of thin crystals, Butterworths, London, 1965.
[27] M.R. Staker, D.L. Holt, The dislocation cell size and dislocation density in copper deformed at temperatures between 25 and 700°C, Acta Metall. 20 (4) (1972) 569–579 https://doi.org/10.1016/0001-6160(72)90012-0.
[28] X. Feaugas, H. Haddou, Grain-size effects on tensile behavior of nickel and AISI 316L stainless steel, Metall. Mater. Trans. A 34 (10) (2003) 2329–2340 https://doi.org/10.1007/s11661-003-0296-5.
[29] X. Feaugas, H. Haddou, Effects of grain size on dislocation organization and internal stresses developed under tensile loading in fcc metals, Philos. Mag. 87 (7) (2007) 989–1018 https://doi.org/10.1080/14786430601019441.
[30] T.G. Gallmeyer, S. Moorthy, B.B. Kappes, M.J. Mills, B. Amin-Ahmadi, A.P. Stebner, Knowledge of process-structure-property relationships to engineer better heat treatments for laser powder bed fusion additive manufactured Inconel 718, Addit. Manuf. 31 (2020) 100977 https://doi.org/10.1016/j.addma.2019.100977.
[31] P. Krakhmalev, G. Fredriksson, K. Svensson, I. Yadroitsev, I. Yadroitsava, M. Thuvander, R. Peng, Microstructure, solidification texture, and thermal stability of 316 L stainless steel manufactured by laser powder bed fusion, Metals 8 (8) (2018) 643 https://doi.org/10.3390/met8080643.
[32] Y. Zhong, L. Liu, J. Zou, X. Li, D. Cui, Z. Shen, Oxide dispersion strengthened stainless steel 316L with superior strength and ductility by selective laser melting, J, Mater. Sci. Technol. (2019) https://doi.org/10.1016/j.jmst.2019.11.004.
[33] G. Meric de Bellefon, K.M. Bertsch, M.R. Chancey, Y.Q. Wang, D.J. Thoma, Influence of solidification structures on radiation-induced swelling in an additively-manufactured austenitic stainless steel, J, Nucl. Mater. 523 (2019) 291–298 https://doi.org/10.1016/j.jnucmat.2019.06.012.
[34] D. Kuhlmann-Wilsdorf, Theory of plastic deformation: - properties of low energy dislocation structures, Mater. Sci. Eng. A 113 (1989) 1–41 http://dx.doi.org/10.1016/0921-5093(89)90290-6.
[35] D. Kuhlmann-Wilsdorf, J.H. Van Der Merwe, Theory of dislocation cell sizes in deformed metals, Mater. Sci. Eng. 55 (1) (1982) 79–83 https://doi.org/10.1016/0025-5416(82)90086-6.
[36] N. Hansen, New discoveries in deformed metals, Metall. Mater. Trans. A 32 (12) (2001) 2917–2935 https://doi.org/10.1007/s11661-001-0167-x.
[37] D.J. Michel, J. Moteff, A.J. Lovell, Substructure of type 316 stainless steel deformed in slow tension at temperatures between 21° and 816°C, Acta Metall. 21 (9) (1973) 1269–1277 https://doi.org/10.1016/0001-6160(73)90168-5.
[38] S.N. Monteiro, H.-J. Kestenbach, Influence of grain orientation on the dislocation substructure in austenitic stainless steel, Metall. Trans. A 6 (4) (1975) 938 https://doi.org/10.1007/bf02672323.
[39] D.L. Holt, Dislocation cell formation in metals, J, Appl. Phys. 41 (8) (1970) 3197–3201 https://doi.org/10.1063/1.1659399.
[40] U.F. Kocks, H. Mecking, Physics and phenomenology of strain hardening: the FCC case, Prog. Mater Sci. 48 (3) (2003) 171–273 https://doi.org/10.1016/S0079-6425(02)00003-8.
[41] D.A. Hughes, Q. Liu, D.C. Chrzan, N. Hansen, Scaling of microstructural parameters: Misorientations of deformation induced boundaries, Acta Mater 45 (1) (1997) 105–112 https://doi.org/10.1016/S1359-6454(96)00153-X.
[42] D.L. McDowell, A perspective on trends in multiscale plasticity, Int. J. Plast. 26 (9) (2010) 1280–1309 https://doi.org/10.1016/j.ijplas.2010.02.008.
[43] H. Mughrabi, On the role of strain gradients and long-range internal stresses in the composite model of crystal plasticity, Mater. Sci. Eng. A 317 (1) (2001) 171–180 https://doi.org/10.1016/S0921-5093(01)01173-X.
[44] D. Kuhlmann-Wilsdorf, N. Hansen, Geometrically necessary, incidental and subgrain boundaries, Scr. Metall. Mater. 25 (7) (1991) 1557–1562 https://doi.org/10.1016/0956-716X(91)90451-6.
[45] T. Mukherjee, H.L. Wei, A. De, T. DebRoy, Heat and fluid flow in additive manufacturing – Part II: Powder bed fusion of stainless steel, and titanium, nickel and aluminum base alloys, Comput. Mater. Sci. 150 (2018) 369–380 https://doi.org/10.1016/j.commatsci.2018.04.027.
[46] T. Mukherjee, W. Zhang, T. DebRoy, An improved prediction of residual stresses and distortion in additive manufacturing, Comput. Mater. Sci. 126 (2017) 360–372 https://doi.org/10.1016/j.commatsci.2016.10.003.
[47] S. Murugesan, P. Kuppusami, E. Mohandas, M. Vijayalakshmi, X-ray diffraction Rietveld analysis of cold worked austenitic stainless steel, Mater. Lett. 67 (1) (2012) 173–176 https://doi.org/10.1016/j.matlet.2011.09.065.